Journal of Power Sources 223 (2013) 246–253

Contents lists available at SciVerse ScienceDirect

Journal of Power Sources

journal homepage: www.elsevier.com/locate/jpowsour

Platinum-catalyzed carbon nanotubes for durability enhancement of low-temperature fuel cells

Byeongchul Ha [a,1], Oc Hee Han [a,b,c,*]

[a] Analysis Research Division, Daegu Center, Korea Basic Science Institute, 1370 Sankyukdong, Bookgu, Daegu 702-701, Republic of Korea
[b] Graduate School of Analytical Science and Technology, Chungnam National University, Daejeon 305-764, Republic of Korea
[c] Department of Chemistry, Kyungpook National University, Daegu 702-701, Republic of Korea

HIGHLIGHTS

- Pt-catalyzed carbon nanotubes (CNT(Pt)) were synthesized in powder form.
- Current-density peak-areas of CNT(Pt) were increased by repeated potential cycles.
- Repeated potential cycles induced the formation of Pt nanoparticles outside CNTs.
- Extremely durable Pt catalytic properties of CNT(Pt) are useful for fuel cells.

GRAPHICAL ABSTRACT

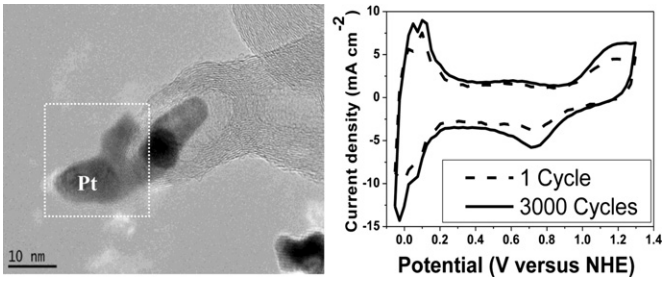

ARTICLE INFO

Article history:
Received 19 July 2012
Received in revised form
10 September 2012
Accepted 11 September 2012
Available online 23 September 2012

Keywords:
Fuel cells
Carbon nanotubes
Platinum
Catalyst
Durability

ABSTRACT

The Pt-catalyzed carbon nanotubes (CNT(Pt)) synthesized in powder form manifests extremely durable Pt catalytic properties. Compared with traditional Pt nanoparticle catalysts, CNT(Pt) exhibits abnormally increased cyclic voltammerty peak areas versus time. This experimental observation not reported previously is explained by the increased catalytic surface areas resulting from newly created crystalline Pt nanoparticles and nanosheets outside carbon nanotubes during repeated potential cycles. CNT(Pt) can initiate a new phase of the research taking an advantage of combined effects of various properties of CNTs (for example, hydrogen-storage capability) and Pt (for example, high catalytic activity).

1. Introduction

Low-temperature fuel cells (LTFCs) are promising candidates as power sources for portable electronic devices and automobiles due to their high power densities and relatively low operating temperatures (~80 °C). However, LTFCs such as direct methanol fuel cells (DMFCs), direct ethanol fuel cells (DEFCs), and proton exchange membrane fuel cells (PEMFCs), have critical problems with durability that must be solved [1–10]. It was revealed that two main factors, the agglomeration and dissolution of Pt particles, used as oxygen reduction reaction (ORR) catalysts in LTFCs, can shorten LTFC lifetime. Highly dispersed Pt nanoparticles supported on carbon have been widely employed as commercial catalysts for LTFCs and have been extensively studied. Pt in nanoparticle morphologies has high surface energies, inducing severe Oswald

* Corresponding author. Analysis Research Division, Daegu Center, Korea Basic Science Institute, 1370 Sankyukdong, Bookgu, Daegu 702-701, Republic of Korea. Tel.: +82 53 950 7912; fax: +82 53 959 3405.
E-mail address: ohhan@kbsi.re.kr (O.H. Han).
[1] Department of Nanosystem and Nanoprocessing Engineering, Pusan National University, Busan 609-735, Republic of Korea.

0378-7753/$ – see front matter © 2012 Elsevier B.V. All rights reserved.
http://dx.doi.org/10.1016/j.jpowsour.2012.09.065

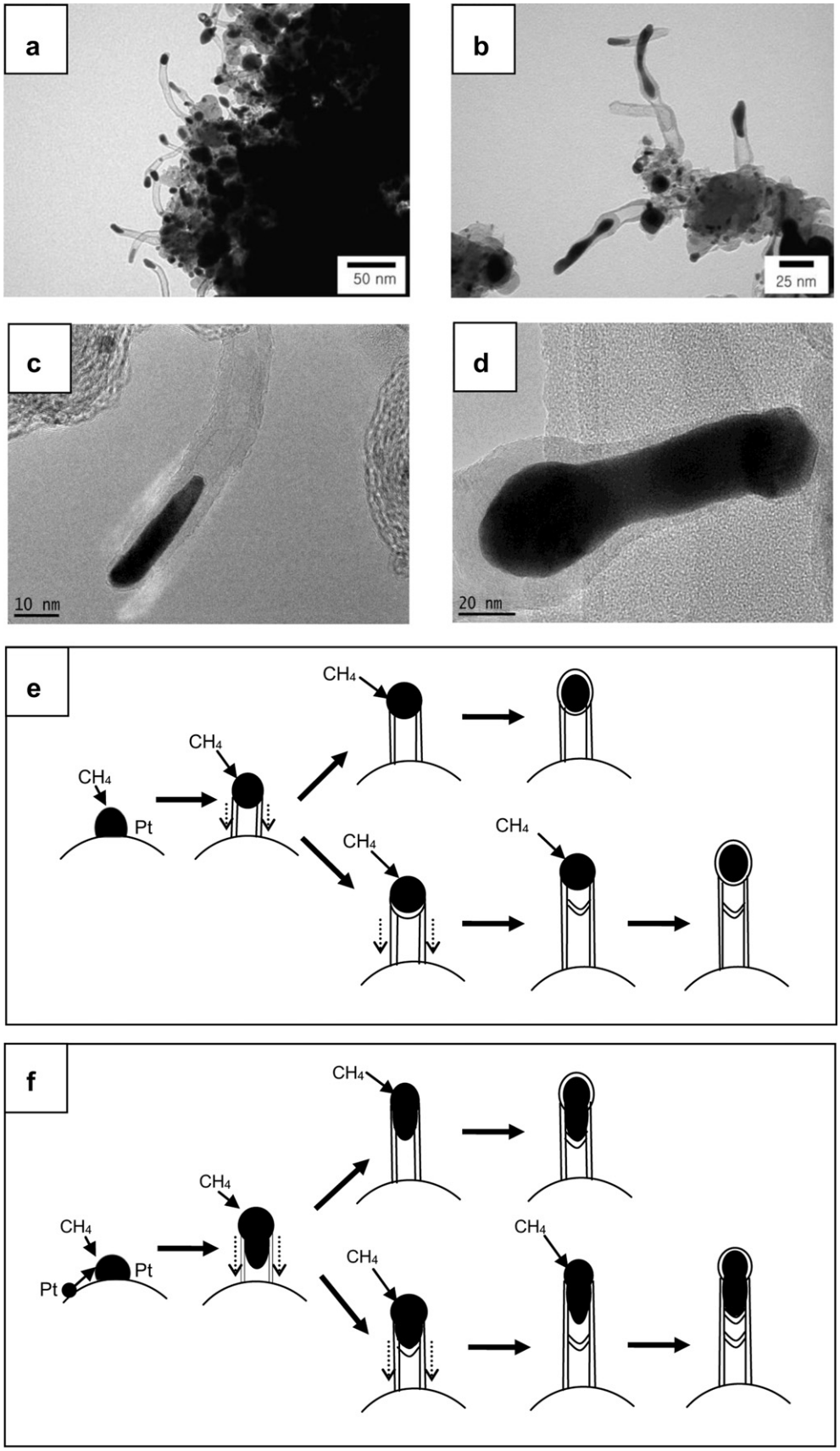

Fig. 1. (a)–(d) TEM images of CNT(Pt). Pt nanoparticles are shown as black spots on the TEM images. Pt tip-growth models of CNTs containing (e) Pt nanoparticles and (f) Pt nanowires.

ripening [3] and grain growth during fuel cell operation. The resulting agglomeration of the Pt nanoparticles degrades catalytic performance due to reduced surface area. Therefore, a key challenge has been improving the long-term stability of Pt catalyst by alleviating the dissolution and agglomeration of highly dispersed Pt nanoparticles. A previous approach to improving catalytic durability used one-dimensional Pt nanowires or nanotubes as catalysts [1–3]. This one-dimensional morphology makes Pt less vulnerable to dissolution and aggregation than Pt nanoparticles during fuel cell operation [3]. Nitrogen-doped Fe-catalyzed carbon nanotubes (CNTs) were also reported to exhibit enhanced catalytic activity and stability as ORR catalysts in LTFCs.

Here we report the first preparation of Pt-catalyzed carbon nanotubes (CNT(Pt)) using Pt nanoparticles supported on Vulcan XC-72 (Pt/C) and methane by chemical vapor deposition (CVD), for ORR catalysts in LTFCs. Unlike previous Pt-catalyzed CNT synthesis [11], our CNT(Pt) was synthesized without flat quartz substrates for the purpose of mass production and easy application as catalysts. In contrast to the CNTs used in CNT(Pt), most CNTs used as supports for Pt nanoparticles have been synthesized by Fe, Ni, or Co nanoparticle catalysts [10]. The nature of the durability and catalytic activity of CNT(Pt) was identified.

2. Experimental

CNT(Pt) was synthesized by CVD using a commercial Pt/C catalyst (E-TEK, 58.2 wt% Pt). To prepare CNT(Pt), Pt/C was placed on an alumina boat inside the quartz tube of a CVD system. A constant argon carrier gas flow of 1000 cm^3 min^{-1} was passed through the quartz tube while temperature was increased from room temperature to 950 °C at 35 °C min^{-1}. Then at 950 °C for 30 min, argon gas flow was replaced with a constant flow of methane gas (99.999%) at 50 cm^3 min^{-1} and of hydrogen gas (99.999%) at 300 cm^3 min^{-1}. After that, heating was stopped and the sample was cooled to room temperature under a constant argon carrier gas flow of 1000 cm^3 min^{-1}. The morphologies and nanostructures of CNT(Pt) were studied by F20 Field Emission TEM (Tecnai, U.S.A.) and S-4800 TEM (Hitachi, Japan). CNT(Pt) is characterized by ESCALAB 250 XPS (VG Scientifics, England), X'Pert APD X-ray diffractometer (Philips, Netherlands), and 1403 Raman spectroscopy (SPEX, Japan) with an Ar-ion laser beam of 514.5 nm. Cyclic voltammetry (CV) data for sample materials loaded onto a Pt boat working electrode, were obtained with a 263A potentiostat/galvanostat (Princeton Applied Research, U.S.A.) by applying 3000 cycles of CV, between −0.053 and 1.297 V, at a scan rate of 50 mV s^{-1}, in an air saturated 0.5 M H_2SO_4 electrolyte solution. All of the potentials experimentally measured with a Ag|AgCl (1M) reference electrode in this work were converted and reported versus the normal hydrogen electrode (NHE). For rotating disk electrode (RDE) experiments, the mixture solution containing 0.002 g CNT(Pt) catalyst, 0.01 g Nafion ionomer solution, and 0.5 g H_2O was prepared. The mixture solution of 5 μl (corresponding to 20 μg CNT(Pt) catalyst) was placed on the polished glassy carbon RDE electrode (Pine Research Instrumentation, U.S.A.) of 0.2 cm^2 and dried. Then, the RDE experiments were performed in an O_2 saturated (99.995% O_2) 0.5 M H_2SO_4 solution at speeds of 200, 400, 800, 1200, and 1600 rpm with a scan rate of 10 mVs^{-1}.

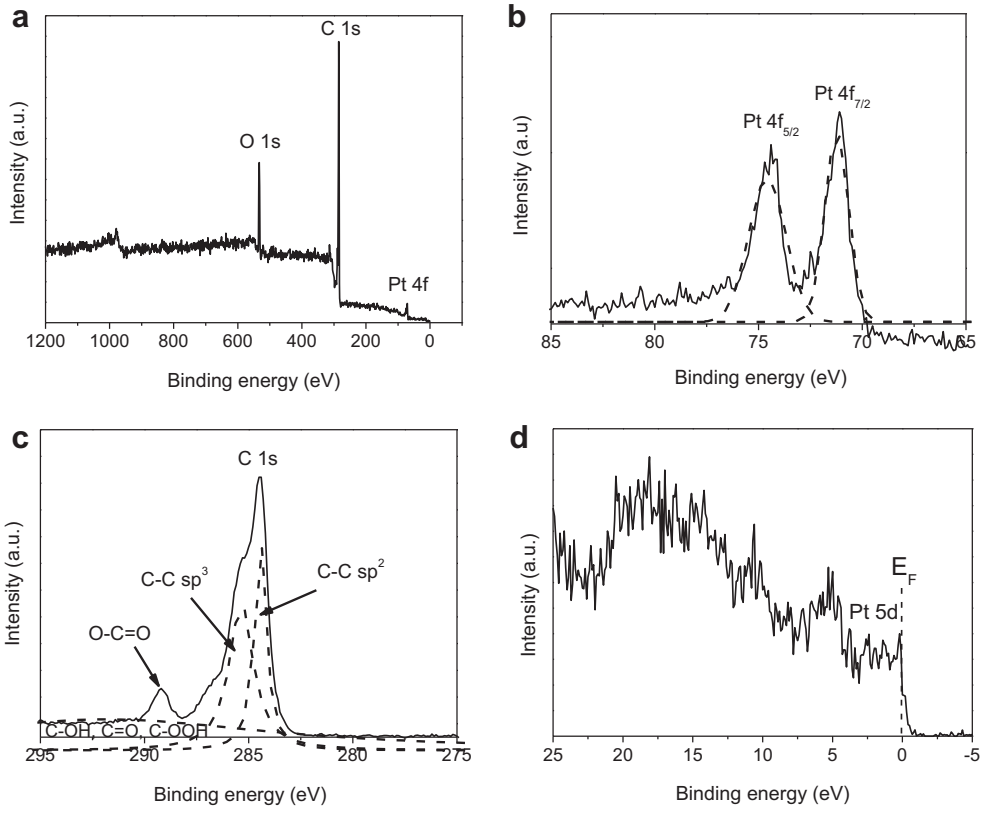

Fig. 2. XPS spectra of CNT(Pt). (a) Whole spectra of CNT(Pt). (b) Pt 4f spectra of CNT(Pt). (c) C 1s spectrum of CNT(Pt) deconvoluted with signals from C–C bonds and oxygen–carbon bonds. (d) Valence band spectra of CNT(Pt). The Fermi level energy of CNT(Pt) was determined with respect to that of Cu foil, defined as the level of zero binding energy.

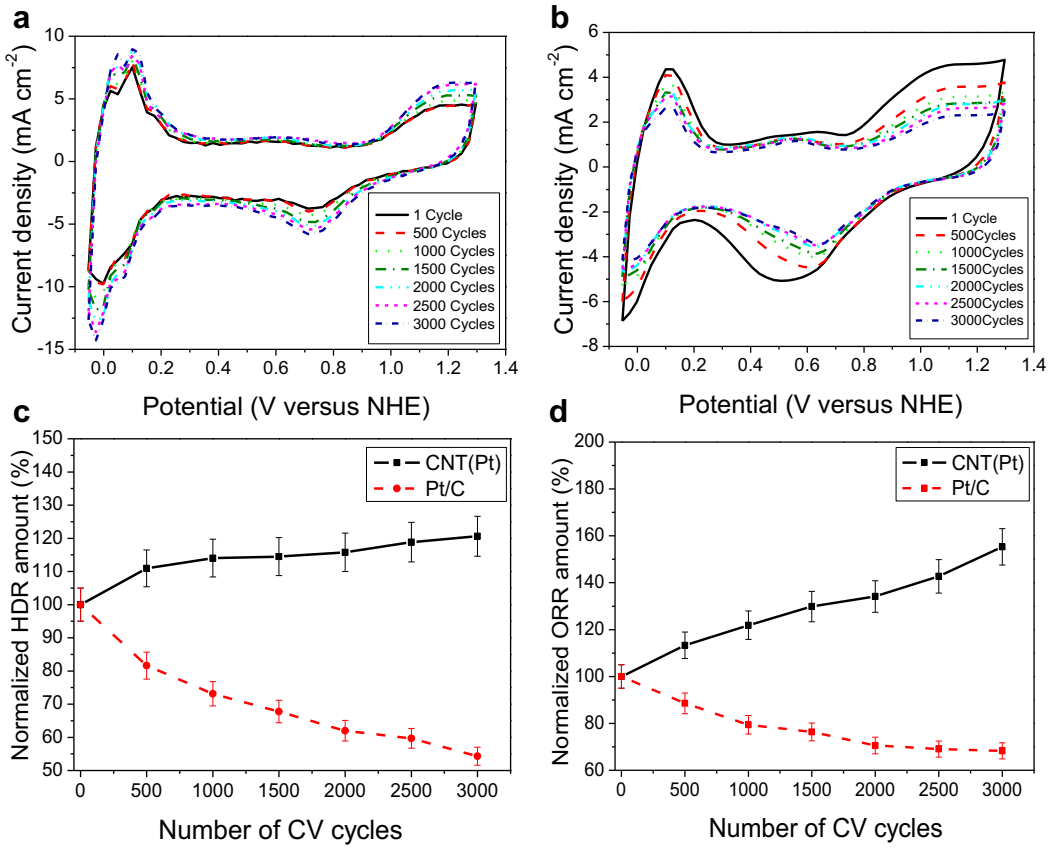

Fig. 3. RPC data of (a) CNT(Pt) and (b) Pt/C catalysts in an air saturated 0.5 M H_2SO_4 solution with a sweep rate of 50 mVs^{-1} at room temperature. (c) HDR amount variation of CNT(Pt) (black solid line) and Pt/C (red dotted line) catalysts as a function of CV cycling numbers. (d) ORR amount variation of CNT(Pt) (black solid line) and Pt/C (red dotted line) catalysts as a function of CV cycling numbers.

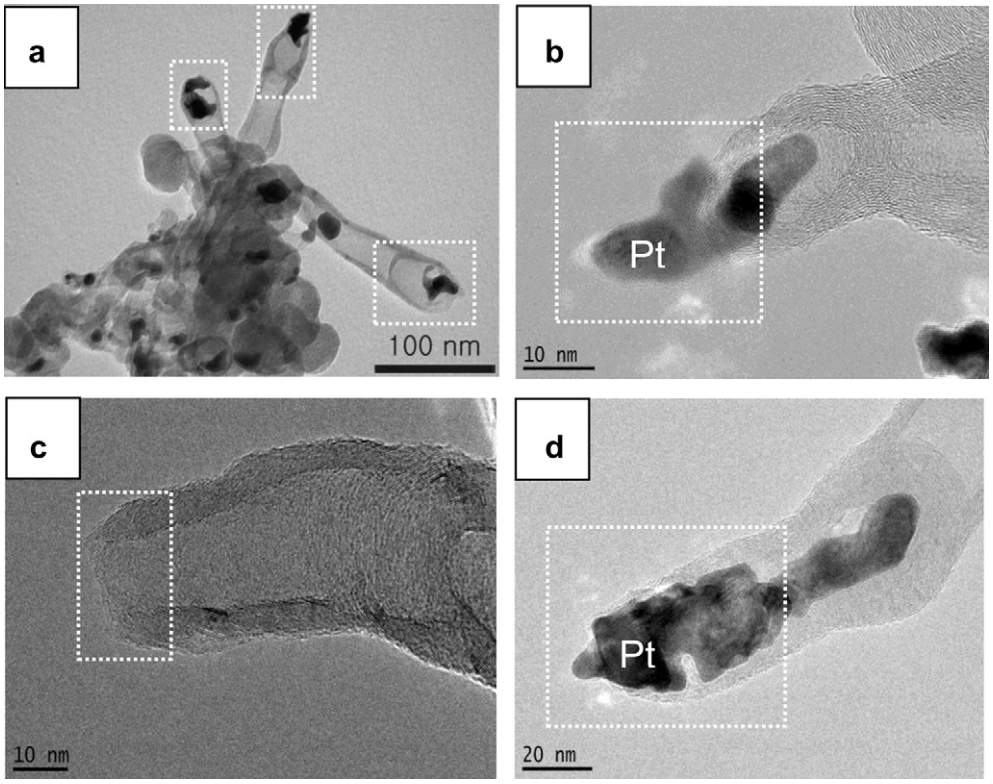

Fig. 4. TEM images of CNT(Pt) after RPC (3000 cycles). (a) Pt nanoparticles (black spots) are diffused through the tip of CNT. Parts of Pt nanoparticles inside of CNTs are migrated to the outside of CNTs so that vacant spaces, previously occupied with Pt nanoparticles, are shown at the tip of CNTs. (b) Pt nanoparticles (black spots) are diffused and migrated through graphene layers of CNT(Pt). (c) Vacant space, which was previously occupied with Pt particles shows a hole at the tip of CNT. (d) Pt nanoparticles are diffused and migrated through the graphene layers of CNT(Pt).

3. Results and discussion

Transmission electron microscopy (TEM) images of CNT(Pt) indicate that the as-synthesized CNT(Pt) have Pt nanoparticles (darker spots in the images in Fig. 1a and b) or Pt nanowires (dark nanowires in the images in Fig. 1b–d) embedded in the tips of the CNTs. TEM results suggest that CNTs were grown from Pt catalysts located at the tips of CNTs via the Vapor–Liquid–Solid (VLS) mechanism [12–17]. The VLS growth mechanism was first developed for the growth of Si nanowires using an Au catalyst, where the Au catalysts are located at the tip of Si nanowires [14,15], as for Pt in CNT(Pt). However, although multiwalled CNTs (MWCNTs) using Fe, Ni, and Co catalysts were also grown via the VLS mechanism, the catalysts remained at the bottom of the MWCNTs [12,13]. In the VLS mechanism for CNT(Pt), as schematically shown in Fig. 1e and f, the Pt catalyst is supersaturated with carbon originating from CH_4 through the chemical reaction of $CH_4 \rightarrow C + 2H_2$, and supersaturated carbon builds CNT walls. The growing CNTs push the Pt catalyst to the tips of the CNTs, and at the end of the reaction, the supersaturated liquid state Pt catalyst solidifies on the tips of CNTs, creating Pt nanoparticles and nanowires inside the CNTs. Consequently, the Pt nanoparticles and nanowires are encapsulated by the solidified supersaturated carbon. Bamboo-shaped CNTs are developed by bamboo-shaped joints grown at the bottom of the Pt catalysts, as shown in Fig. 1b, e and f.

The X-ray spectroscopy (XPS) spectrum of the CNT(Pt) in Fig. 2a shows 87.67 atomic % (at.%) C, 0.36 at.% Pt, and 11.96 at.% O. The increased carbon content of CNT(Pt) suggests the added carbons from CH_4 source. However, the Pt content of CNT(Pt) was probably underestimated by XPS due to the fact that the Pt of CNT(Pt) is encapsulated by carbon layers and XPS has a shallow penetration depth. The Pt 4f band energy region was deconvoluted to Pt $4f_{7/2}$ and Pt $4f_{5/2}$ signals in Fig. 2b. The C 1s energy region of CNT(Pt) identifies sp^2 and sp^3 C–C bonds and oxygen containing functional groups such as O–C=O, C–OH, C=O, and C–OOH as shown in Fig. 2c. The XPS spectrum in Fig. 2d shows that the Pt 5d band provides the main contribution to the valence band near the Fermi energy of CNT(Pt). The valence band characteristics, especially those of Pt 5d bands near the Fermi energy, must play an essential role in determining the catalytic reactivity because the valence band, especially Pt 5d band, directly correlates with the catalytic activity for the ORR [18].

Accelerated durability tests (ADT) of CNT(Pt) and Pt/C catalysts were conducted by RPC in an air saturated 0.5 M H_2SO_4 solution at a scan rate of 50 mVs^{-1} and room temperature, as shown in Fig. 3a and b, respectively. Interestingly, the hydrogen desorption reaction (HDR) peak areas (measured between 0.05 V and 0.4 V in anodic scans) of the CNT(Pt) catalysts were gradually enhanced to 120 ± 5% of the initial peak areas after 3000 cycles, whereas the HDR peak areas of the Pt/C catalysts were dramatically reduced to 54 ± 5% of the initial peak areas (Fig. 3c). Most Pt catalysts treated by RPC have been reported to have the reduction of HDR peak areas [19–24] due to dissolution and aggregation of Pt catalysts, as observed with Pt/C in this work. The increased HDR peak area of Pt by RPC observed in this work has never been reported. Fig. 3d exhibits that the ORR peak areas of CNT(Pt) gradually increased up to 155 ± 5%, whereas those of Pt/C decreased to 68 ± 5% after 3000 cycles. The increased ORR (measured between 0.6 V and 0.85 V in cathodic scans) and HDR peak areas of CNT(Pt) are tentatively attributed to the increased active sites of Pt, while Pt of Pt/C lost the active sites due to dissolution and aggregation of Pt catalysts. Therefore, the electrocatalytic activity for ORR (consequently, activity lifetime as well) of CNT(Pt) and Pt/C were significantly enhanced and reduced, respectively, by RPC.

The morphological change of CNT(Pt) due to RPC was investigated by TEM (Fig. 4). Comparing the TEM images in Figs. 1b and 4a indicates that the Pt-catalyst diameter in CNT(Pt) decreased slightly, and the Pt-catalyst surfaces became rough after RPC. In addition, Fig. 4a–d suggests that Pt catalysts migrated to the outside of CNT(Pt) through the tips of CNT(Pt). Consequently, the Pt catalytic surface area not covered by carbon layers is increased. This migration of Pt through the tip of CNTs has not been reported even though the formation of Pt particles in Nafion polymer electrolyte membranes in LTFCs [25–27] has been observed. The latter observation was explained that the Pt ions that dissolved from the cathode electrode diffused and reduced to metal Pt particles in the membranes. The observed Pt migration in CNT(Pt) probably occurred through a similar mechanism composed of dissolved Pt turning into Pt ions and the reduction of Pt ions to Pt metal particles (oxidation of Pt to Pt^{z+} ($z = 2, 4$) ions, hydrogen oxidation and simultaneous reduction of Pt^{z+} ions to Pt during RPC) [22]. However, the introduction of one-dimensional CNTs wrapping the Pt nanoparticles to CNT(Pt) considerably alleviated the dissolution and aggregation of the Pt particles. On the other hand, Pt particles of Pt/C grew as reported previously [3,7], confirming that the major cause for the CV peak area loss of Pt/C catalysts was Pt particle growth by Ostwald ripening [3,7,22,24]. The size distributions of Pt nanoparticles before and after RPC (Fig. 5a) were also measured using TEM images. The populations of small Pt nanosheets or Pt nanoparticles less than 5-nm in length or diameter increased after RPC as the Pt ions from Pt particles in CNT(Pt) turned into Pt nanosheets or nanoparticles outside of

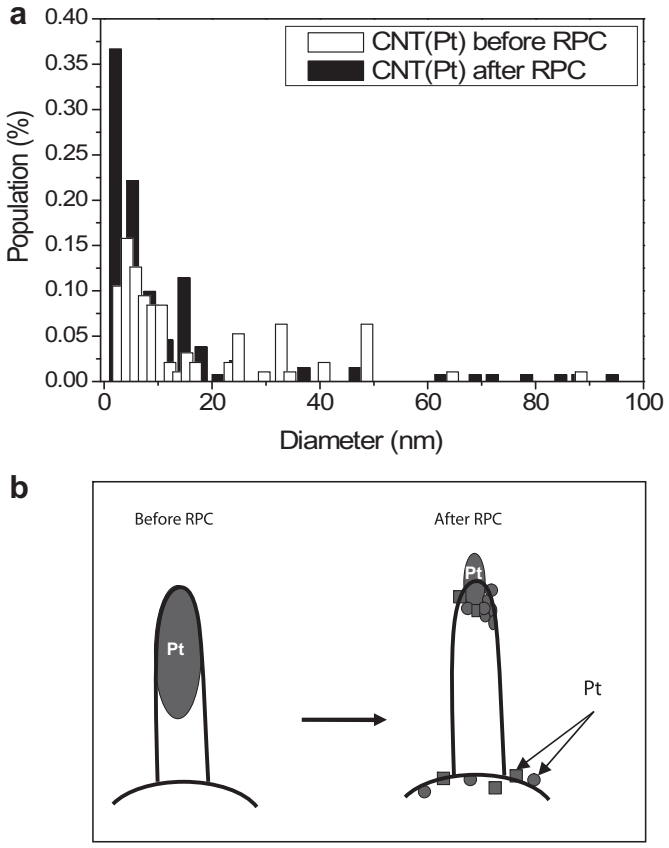

Fig. 5. (a) The size (presented in diameter) distribution of Pt nanoparticles of CNT(Pt) before and after RPC. (b) Schematic diagram of smaller sized Pt nanoparticle formation out of CNT(Pt). Small circles and squares stand for the Pt nanoparticles and nanosheets, respectively.

CNTs. The scheme of this process is shown in Fig. 5b. Production of Pt nanosheets or nanoparticles outside of CNTs was confirmed by XRD patterns showing split signals after RPC with JCPDS analysis (Fig. 6) [28]. The population ratio of Pt nanoparticles to Pt nanosheets (signals shifted to larger angles) was approximately 1:1. XRD patterns of as-synthesized CNT(Pt), obtained with Cu K_α radiation at $\lambda = 1.542$ Å, show characteristic signals of Pt nanoparticles at 39.75°, 46.23°, 69.20°, 81.25° and 85.76°, identifying Pt(111), Pt(200), Pt (220), Pt(311), and Pt(222) crystal planes, respectively (Fig. 6). The Pt crystallites of CNT(Pt) before and after RPC were in face-centered cubic (FCC) structures, while the average size of Pt crystallites changed from 0.66 nm to 1.19 nm nanoparticles and 0.29 nm nanosheets, as calculated with Pt(111) data using Scherrer's equation [29]. The Raman spectra of CNT(Pt), even after RPC (Fig. 7), mainly show three characteristic Raman bends of MWCNTs, D (at 1355.5 cm^{-1}), G (at 1597.2 cm^{-1}), and second order (at 2699.6 cm^{-1}) bands not drastically different from those (at 1347.4, 1587.9, and 2661.5 cm^{-1}) of CNT(Pt) before RPC [30], indicating that the CNTs of CNT(Pt) remained as MWCNTs even after RPC. Thus, the increased CV peak areas of CNT(Pt) after RPC demonstrate that the durability of CNT(Pt) is better than that of CNT(M) (M = Fe, Ni, or Co) [1]. This is a result of the decreased

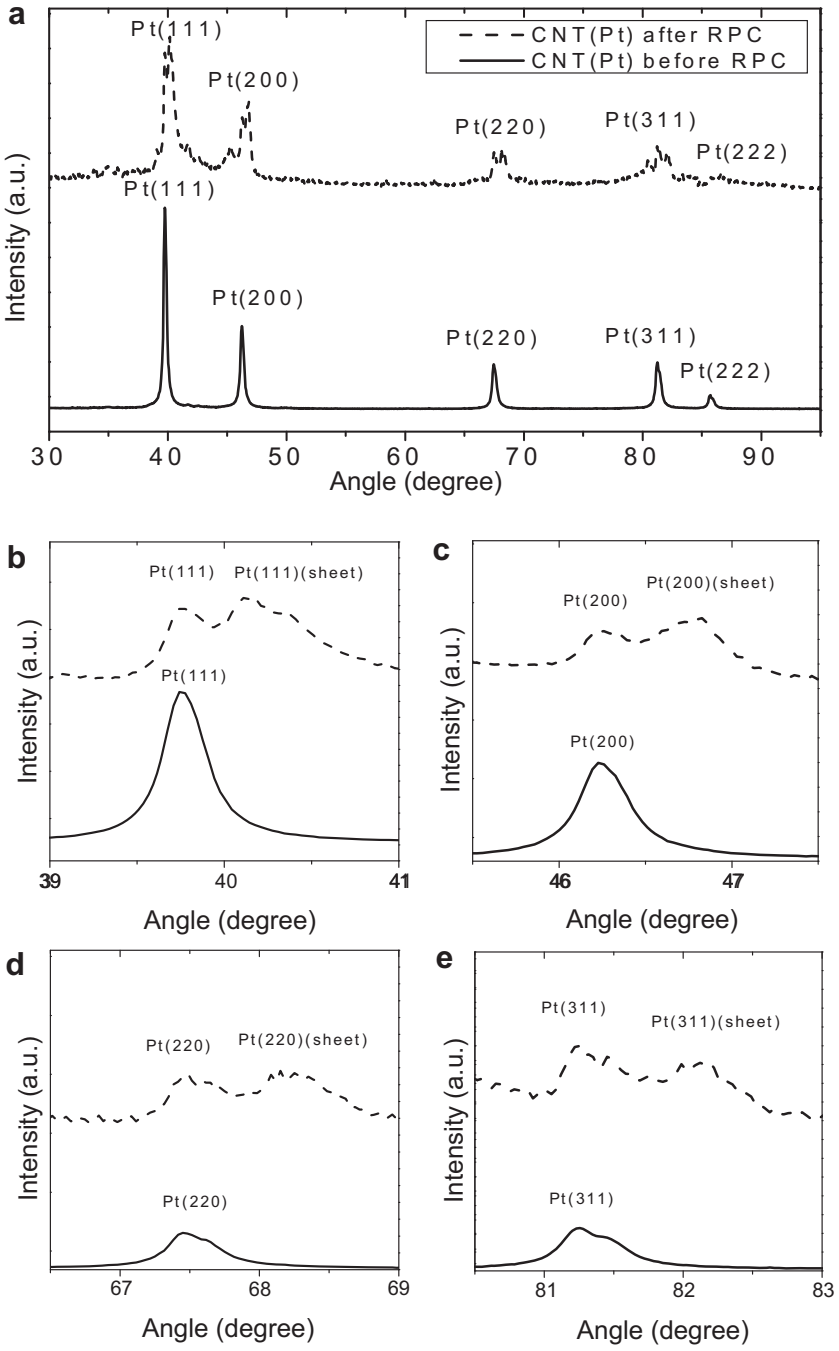

Fig. 6. (a) Whole XRD spectra of CNT(Pt) before and after RPC (3000 cycles) and XRD spectra for each crystalline plane such as (b) Pt(111), (c) Pt(200), (d) Pt(220), and (e) Pt(311) of CNT(Pt) before and after RPC. The solid and dotted lines indicate the XRD spectra before and after RPC, respectively.

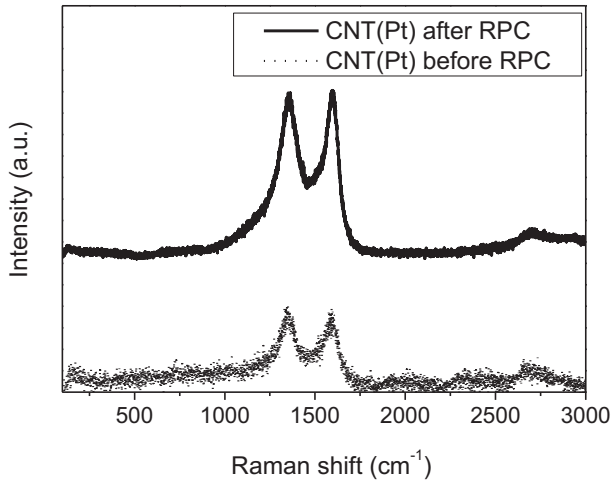

Fig. 7. Raman spectra of CNT(Pt) before and after RPC (3000 cycles) drawn with the dotted (bottom) and solid (top) lines, respectively.

dissolution of Pt of CNT(Pt) compared to M of CNT(M) in an 0.5 M H_2SO_4 solution during RPC.

The rotating disk electrode (RDE) data in Fig. 8 show that ORR activity of CNT(Pt) before and after RPC was enhanced by disk rotation speed. In the slopes of Koutecky–Levich (K–L) plots [31] in Fig. 8b and d, it can be seen that the number of electrons transferred per O_2 molecule (n) was about 2 before and after RPC, resulting from the two-electron oxygen reduction processes producing H_2O_2 ($O_2 + 2H^+ + 2e^- \rightarrow H_2O_2$). The rate constant ($k_2$) for the reaction at CNT(Pt) after RPC, calculated from K–L plot intercepts, was 5.02×10^{-2} cm s^{-1}, which is 5.1 times greater than that of CNT(Pt) before RPC (9.82×10^{-3} cm s^{-1}). Because the reaction rate is proportional to the number of active sites and/or the turnover rate [32], the number of active Pt surface sites and/or the turnover rate at catalytic sites of CNT(Pt) must have increased during RPC. This is in agreement with the enhanced Pt surface sites expected from the increased numbers of Pt nanoparticles and nanosheets less than 5 nm outside of the CNTs (Fig. 5a). However, the greater enhancement of the reaction rate than the increased HDR amount (~20%), which is proportional to the increased active surface sites, indicates the enhanced turnover rate of CNT(Pt) after RPC. The variation of the turnover rate for CNT(Pt) is probably due to the difference of the turnover rates on Pt outside and inside of CNTs. As the more Pt is present outside CNTs, the average turnover rate calculated with the turnover rates of Pt outside and inside of CNTs is expected to be larger.

4. Conclusions

In conclusion, CNT(Pt) synthesized by a CVD method using CH_4 gas and Pt/C in powder form manifests highly durable Pt catalytic properties. RPC treatment results in the production of smaller Pt particles not covered by CNTs out of the Pt nanoparticles encapsulated by CNTs. Our results suggest that the durability of Pt nanoparticle catalysts can be improved by locating Pt nanoparticles

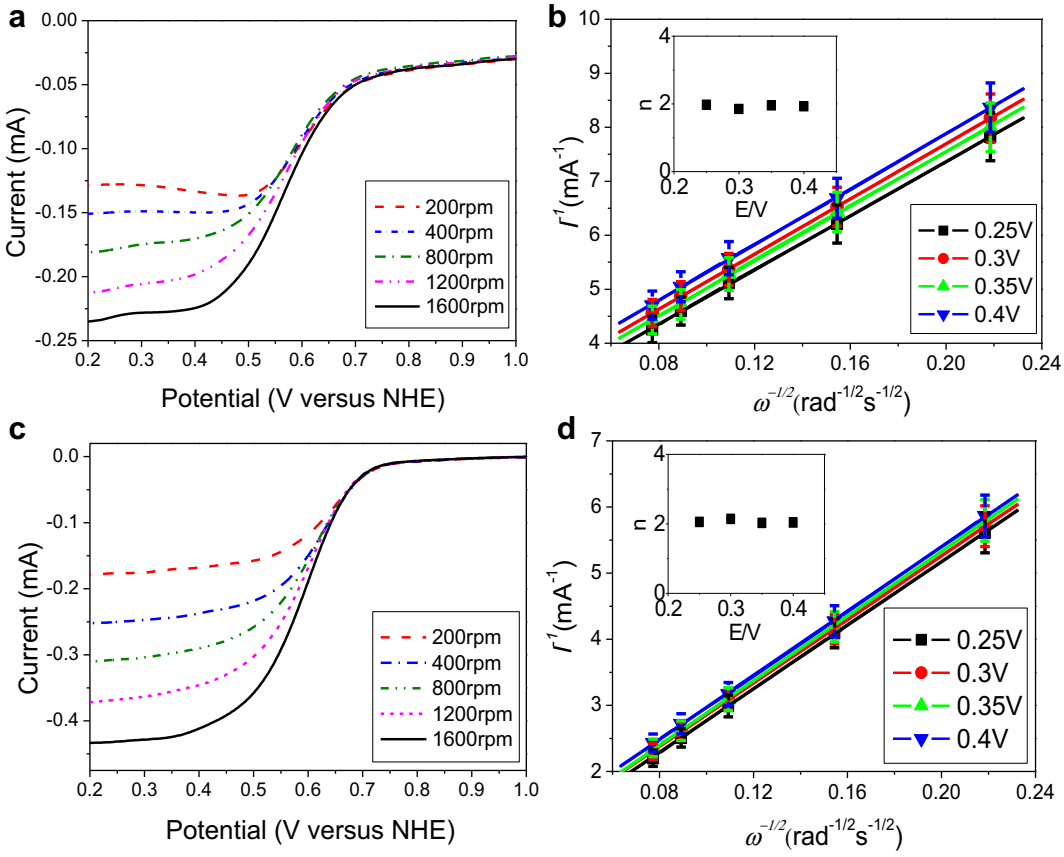

Fig. 8. (a) RDE data of CNT(Pt) before RPC with the scan rate of 10 mVs^{-1} at the rotating speed of 100, 200, 400, 800, and 1600 rpm. (b) K–L plot of CNT(Pt) before RPC. (c) RDE data of CNT(Pt) after RPC with the scan rate of 10 mVs^{-1} at the rotating speed of 100, 200, 400, 800, and 1600 rpm. (d) K–L plot of CNT(Pt) after RPC. The insets show the number of electrons transferred per O_2 molecule (n).

inside of one-dimensional CNTs and by making the Pt nanoparticles subsequently released from the CNT tips as smaller particles during usage of the catalysts. As mass production of CNT(Pt) in powder form is possible, CNT(Pt) can be used as catalysts with enhanced durability in various applications such as LTFCs [10], bio-sensors [33], bio-electronics [33], electrochemical sensors [34], microbio fuel cells [35,36], drug delivery systems for a cancer [37], and hydrogen-storage systems [38]. Furthermore, CNT(Pt) can initiate a new phase of the research taking an advantage of combined effects of various properties of CNTs (for example, hydrogen-storage capability [1,38]) and Pt (for example, high catalytic activity).

Acknowledgements

This work was supported by the KBSI grants (K29030 and K31030) to Dr. O.H. Han and by the National Research Foundation of Korea Grant funded by the Korean Ministry of Education, Science and Technology (2012, University-Institute cooperation program). The authors acknowledge Mr. K.J. Hwang, Dr. W.-J. Moon, Dr. S.G. Lee, Dr. S.-H. Jeong, and Dr. J.S. Bae at the KBSI for acquiring TEM, HR-TEM, XRD, Raman, and XPS data, respectively.

References

[1] K. Gong, F. Du, Z. Xia, M. Durstock, L. Dai, Science 323 (2009) 760–764.
[2] Z. Chen, M. Waje, W. Li, Y. Yan, Angew. Chem. Int. Ed. 46 (2009) 4060–4063.
[3] S. Sun, G. Zhang, D. Geng, Y. Chen, R. Li, M. Cai, X. Sun, Angew. Chem. Int. Ed. 50 (2011) 422–426.
[4] Z. Peng, H. Yang, J. Am. Chem. Soc. 131 (2009) 7542–7543.
[5] H.A. Gasteiger, N.M. Marković, Science 324 (2009) 48–49.
[6] S.-Y. Huang, P. Ganesan, S. Park, B.N. Popov, J. Am. Chem. Soc. 131 (2009) 13898–13899.
[7] K.S. Han, O.H. Han, P.K. Babu, Electrochim. Acta 152 (2005) J131–J135.
[8] Y. Paik, S.-S. Kim, O.H. Han, Angew. Chem. Int. Ed. 47 (2008) 94–96.
[9] I. Kim, O.H. Han, S.A. Chae, Y. Paik, S.-H. Kwon, K.-S. Lee, Y.-E. Sung, H. Kim, Angew. Chem. Int. Ed. 50 (2011) 2270–2274.
[10] C. Wang, M. Waje, X. Wang, J.M. Tang, R.C. Haddon, Y. Yan, Nano Lett. 4 (2004) 345–348.
[11] D. Yuan, L. Ding, H. Chu, Y. Feng, T.P. McNicholas, J. Liu, Nano Lett. 8 (2008) 2576–2579.
[12] J.A. Rodríguez-Manzo, M. Terrones, H. Twrrones, H.W. Kroto, H.L. Sun, F. Banhart, Nat. Nanotech. 2 (2007) 307–311.
[13] C.J. Lee, J. Park, Appl. Phys. Lett. 77 (2000) 3397–3399.
[14] A.M. Morales, C.M. Lieber, Science 279 (1998) 208–211.
[15] R.S. Wagner, W.C. Ellis, Appl. Phys. Lett. 4 (1964) 89–90.
[16] S. Helveg, C. López-Cartes, J. Sehested, P.L. Hansen, B.S. Clausen, J.R. Rostrup-Nielsen, F. Abild-Pedersen, J.K. Nørskov, Nature 427 (2004) 426–429.
[17] B. Ha, C.J. Lee, Appl. Phys. Lett. 90 (2007) 023108.
[18] B. Ha, O.H. Han, K.J. Hwang, S. Kim, C.K. Rhee, Electrochim. Acta 58 (2011) 422–426.
[19] V. Stamenkovic, B.S. Mun, K.K.J. Mayrhofer, P.N. Ross, N.M. Marković, J. Rossmeisl, J. Greeley, J.K. Nørskov, Angew. Chem. Int. Ed. 45 (2006) 2897–2901.
[20] V.R. Stamenkovic, B.J. Mun, M. Arez, K.J.J. Mayrhofer, C.A. Lucas, G. Wang, P.N. Ross, N.M. Marković, Nat. Mater. 6 (2007) 241–247.
[21] M. Nogami, R. Koike, R. Jalem, G. Kawamura, Y. Yang, Y. Sasaki, J. Phys. Chem. Lett. 1 (2010) 568–571.
[22] R. Borup, J. Meyers, B. Pivovar, Y.S. Kim, R. Mukundan, N. Garland, D. Myers, M. Wilson, F. Garzon, D. Wood, P. Zelenay, K. More, K. Stroh, T. Zawodzinski, X.J. Boncella, J.E. McGrath, O.M. Inaba, K. Miyatake, M. Hori, K. Ota, Z. Ogumi, S. Miyata, A. Nishikata, Z. Siroma, Y. Uchimoto, K. Yasuda, K. Kimijima, N. Iwashita, Chem. Rev. 107 (2007) 3904–3951.
[23] B. Lim, M. Jiang, P.H.C. Camargo, E.C. Cho, J. Tao, X. Lu, Y. Zhu, Y. Xia, Science 324 (2009) 1302–1305.
[24] T. Fuller, C. Hartnig, V. Ramani, H. Uchida, H.A. Gasteiger, S. Cleghorn, P. Strasser, T. Zawodzinski, D. Jones, P. Shirvanian, T. Jarvi, P. Zelenay, C. Lamy, P. Bele (Eds.), Proton Exchange Membrane Fuel Cells 9, vol. 25, ECS Transactions, New Jersey, U.S.A, 2009, pp. 573–581.
[25] W. Bi, T.F. Fuller, J. Power Sources 178 (2008) 188–196.
[26] W. Bi, G.E. Gray, T.F. Fuller, Electrochem. Solid-State Lett. 10 (2007) B101–B104.
[27] S.G. Rinaldo, J. Stumper, M. Eikerling, J. Phys. Chem. C 114 (2010) 5773–5785.
[28] V.N. Uspenski, S. Konobejewski, Z. Phys. 16 (1923) 215–227.
[29] A.L. Patterson, Phys. Rev. 56 (1939) 978–982.
[30] A. Jorio, M.A. Pimenta, A.G.S. Filho, R. Saito, G. Dresselhaus, M.S. Dresselhaus, New J. Phys. 5 (2003) 139.1–139.17.
[31] N. Alexeyeva, K. Tammeveski, Electrochem. Solid-State Lett. 10 (2007) F18–F21.
[32] L.E. Briand, W.E. Farneth, I.E. Wachs, Catal. Today 62 (2000) 219–229.
[33] J. Ryu, H.-S. Kim, H.T. Hahn, D. Lashmore, Biosens. Bioelectron. 25 (2010) 1603–1608.
[34] S. Hrapovic, Y. Liu, K.B. Male, J.J.T. Luong, Anal. Chem. 76 (2004) 1083–1088.
[35] D. Ivnitsk, B. Branch, P. Atanassov, C. Apblett, Electrochem. Commun. 8 (2006) 1204–1210.
[36] V. Soukharev, N. Mano, A. Heller, J. Am. Chem. Soc. 126 (2004) 8368–8369.
[37] R.P. Feazell, N. Nakayama-Ratchford, H. Dai, S.J. Lippard, J. Am. Chem. Soc. 129 (2007) 8438–8439.
[38] A.C. Dillon, K.M. Jones, T.A. Bekkedahl, C.H. Kiang, D.S. Bethune, M.J. Heben, Nature 386 (1997) 377–379.